

Spatial light interference microscopy (SLIM)

Zhuo Wang,¹ Larry Millet,² Mustafa Mir,¹ Huafeng Ding,¹ Sakulsuk Unarunotai,³
John Rogers,^{3,4} Martha U. Gillette,² and Gabriel Popescu^{1,*}

¹Quantitative Light Imaging Laboratory, Department of Electrical and Computer Engineering, Beckman Institute for Advanced Science & Technology, University of Illinois at Urbana-Champaign, Urbana, Illinois 61801, USA

²Department of Cell and Developmental Biology, University of Illinois at Urbana-Champaign, Urbana, Illinois 61801, USA

³Department of Chemistry, University of Illinois at Urbana-Champaign, Urbana, Illinois 61801, USA

⁴Department of Materials Science and Engineering, University of Illinois at Urbana-Champaign, Urbana, Illinois 61801, USA

*gpopescu@illinois.edu

Abstract: We present spatial light interference microscopy (SLIM) as a new optical microscopy technique, capable of measuring nanoscale structures and dynamics in live cells via interferometry. SLIM combines two classic ideas in light imaging: Zernike's *phase contrast microscopy*, which renders high contrast intensity images of transparent specimens, and Gabor's *holography*, where the phase information from the object is recorded. Thus, SLIM reveals the intrinsic contrast of cell structures and, in addition, renders quantitative optical path-length maps across the sample. The resulting topographic accuracy is comparable to that of atomic force microscopy, while the acquisition speed is 1,000 times higher. We illustrate the novel insight into cell dynamics via SLIM by experiments on primary cell cultures from the rat brain. SLIM is implemented as an add-on module to an existing phase contrast microscope, which may prove instrumental in impacting the light microscopy field at a large scale.

©2011 Optical Society of America

OCIS codes: (180.3170) Interference microscopy; (180.0180) Microscopy; (999.9999) Quantitative phase imaging.

References and links

1. F. Zernike, "How I discovered phase contrast," *Science* **121**(3141), 345–349 (1955).
2. G. Popescu, "Quantitative phase imaging of nanoscale cell structure and dynamics," in *Methods in Cell Biology*, P. J. Bhanu, ed. (Elsevier, 2008), p. 87.
3. D. Paganin, and K. A. Nugent, "Noninterferometric phase imaging with partially coherent light," *Phys. Rev. Lett.* **80**(12), 2586–2589 (1998).
4. D. Zicha, and G. A. Dunn, "An Image-Processing System For Cell Behavior Studies In Subconfluent Cultures," *J. Microsc.* **179**, 11–21 (1995).
5. C. H. Yang, A. Wax, R. R. Dasari, and M. S. Feld, "Phase-dispersion optical tomography," *Opt. Lett.* **26**(10), 686–688 (2001).
6. M. A. Choma, A. K. Ellerbee, C. H. Yang, T. L. Creazzo, and J. A. Izatt, "Spectral-domain phase microscopy," *Opt. Lett.* **30**(10), 1162–1164 (2005).
7. C. Joo, T. Akkin, B. Cense, B. H. Park, and J. F. de Boer, "Spectral-domain optical coherence phase microscopy for quantitative phase-contrast imaging," *Opt. Lett.* **30**(16), 2131–2133 (2005).
8. W. S. Rockward, A. L. Thomas, B. Zhao, and C. A. Dimarzio, "Quantitative phase measurements using optical quadrature microscopy," *Appl. Opt.* **47**(10), 1684–1696 (2008).
9. G. Popescu, T. Ikeda, R. R. Dasari, and M. S. Feld, "Diffraction phase microscopy for quantifying cell structure and dynamics," *Opt. Lett.* **31**(6), 775–777 (2006).
10. T. Ikeda, G. Popescu, R. R. Dasari, and M. S. Feld, "Hilbert phase microscopy for investigating fast dynamics in transparent systems," *Opt. Lett.* **30**(10), 1165–1167 (2005).
11. G. Popescu, L. P. Deflores, J. C. Vaughan, K. Badizadegan, H. Iwai, R. R. Dasari, and M. S. Feld, "Fourier phase microscopy for investigation of biological structures and dynamics," *Opt. Lett.* **29**(21), 2503–2505 (2004).
12. B. Q. Chen, and J. J. Stamnes, "Validity of diffraction tomography based on the first born and the first rytov approximations," *Appl. Opt.* **37**(14), 2996–3006 (1998).
13. G. Gbur, and E. Wolf, "Relation between computed tomography and diffraction tomography," *J. Opt. Soc. Am. A* **18**(9), 2132–2137 (2001).
14. P. S. Carney, E. Wolf, and G. S. Agarwal, "Diffraction tomography using power extinction measurements," *J. Opt. Soc. Am. A* **16**(11), 2643–2648 (1999).

15. V. Lauer, "New approach to optical diffraction tomography yielding a vector equation of diffraction tomography and a novel tomographic microscope," *J. Microsc.* **205**(2), 165–176 (2002).
16. A. M. Zysk, J. J. Reynolds, D. L. Marks, P. S. Carney, and S. A. Boppart, "Projected index computed tomography," *Opt. Lett.* **28**(9), 701–703 (2003).
17. F. Charrière, N. Pavillon, T. Colomb, C. Depeursinge, T. J. Heger, E. A. D. Mitchell, P. Marquet, and B. Rappaz, "Living specimen tomography by digital holographic microscopy: morphometry of testate amoeba," *Opt. Express* **14**(16), 7005–7013 (2006).
18. F. Charrière, A. Marian, F. Montfort, J. Kuehn, T. Colomb, E. Cuhe, P. Marquet, and C. Depeursinge, "Cell refractive index tomography by digital holographic microscopy," *Opt. Lett.* **31**(2), 178–180 (2006).
19. W. Choi, C. Fang-Yen, K. Badizadegan, S. Oh, N. Lue, R. R. Dasari, and M. S. Feld, "Tomographic phase microscopy," *Nat. Methods* **4**(9), 717–719 (2007).
20. G. Popescu, T. Ikeda, K. Goda, C. A. Best-Popescu, M. Laposata, S. Manley, R. R. Dasari, K. Badizadegan, and M. S. Feld, "Optical measurement of cell membrane tension," *Phys. Rev. Lett.* **97**(21), 218101 (2006).
21. Y. K. Park, M. Diez-Silva, G. Popescu, G. Lykotrafitis, W. Choi, M. S. Feld, and S. Suresh, "Refractive index maps and membrane dynamics of human red blood cells parasitized by *Plasmodium falciparum*," *Proc. Natl. Acad. Sci. U.S.A.* **105**(37), 13730–13735 (2008).
22. Y. K. Park, C. A. Best, K. Badizadegan, R. R. Dasari, M. S. Feld, T. Kuriabova, M. L. Henle, A. J. Levine, and G. Popescu, "Measurement of red blood cell mechanics during morphological changes," *Proc. Nat. Acad. Sci.* (2010).
23. G. Popescu, Y. Park, N. Lue, C. Best-Popescu, L. Deflores, R. R. Dasari, M. S. Feld, and K. Badizadegan, "Optical imaging of cell mass and growth dynamics," *Am. J. Physiol. Cell Physiol.* **295**(2), C538–C544 (2008).
24. N. Lue, G. Popescu, T. Ikeda, R. R. Dasari, K. Badizadegan, and M. S. Feld, "Live cell refractometry using microfluidic devices," *Opt. Lett.* **31**(18), 2759–2761 (2006).
25. H. Ding, F. Nguyen, S. A. Boppart, and G. Popescu, "Optical properties of tissues quantified by Fourier-transform light scattering," *Opt. Lett.* **34**(9), 1372–1374 (2009).
26. D. Gabor, "A new microscopic principle," *Nature* **161**(4098), 777–778 (1948).
27. J. B. Pawley, *Handbook of biological confocal microscopy* (Springer, New York, 2006).
28. Z. Wang, and G. Popescu, "Quantitative phase imaging with broadband fields," *Appl. Phys. Lett.* **96**(5), 051117 (2010).
29. Z. Wang, I. S. Chun, X. L. Li, Z. Y. Ong, E. Pop, L. Millet, M. Gillette, and G. Popescu, "Topography and refractometry of nanostructures using spatial light interference microscopy," *Opt. Lett.* **35**(2), 208–210 (2010).
30. C. L. Waites, A. M. Craig, and C. C. Garner, "Mechanisms of vertebrate synaptogenesis," *Annu. Rev. Neurosci.* **28**(1), 251–274 (2005).
31. H. F. Ding, and G. Popescu, "Diffraction phase contrast microscopy," *Opt. Express* **18**(2), 1569–1575 (2010).

1. Introduction

Most living cells do not absorb or scatter light significantly, i.e. they are essentially transparent, or phase objects. Phase contrast microscopy proposed by Zernike represented a major advance in intrinsic contrast imaging, as it revealed inner details of transparent structures without staining or tagging [1]. While phase contrast is sensitive to minute optical path-length changes in the cell, down to the nanoscale, the information retrieved is only qualitative. Quantifying cell-induced shifts in the optical path-lengths permits nanometer scale measurements of structures and motions in a non-contact, non-invasive manner [2]. Thus, quantitative phase imaging (QPI) has recently become an active field of study and various experimental approaches have been proposed [3–11]. Advances in phase-sensitive measurements enabled optical tomography of transparent structures, following reconstruction algorithms borrowed from X-ray computed imaging, in which scattering and diffraction effects are assumed to be negligible [12–16]. Further, QPI-based projection tomography has been applied to live cells [17–19].

Despite these significant technological advances, the range of QPI applications in biology has been largely limited to red blood cell imaging [20–22] or assessment of *global* cell parameters such as dry mass [4,23], average refractive index [24], and statistical parameters of tissue slices [25]. This limitation is due to two main reasons, as follows. First, because of speckle generated by the high temporal coherence of the light used (typically lasers), the contrast in QPI images has never matched that exhibited in *white light* techniques such as phase contrast and Nomarski. Second, the experimental setups tend to be rather complex, of high maintenance, which limits their in-depth biological applicability.

Here, we present SLIM as a novel, highly sensitive QPI method, which promises to enable unprecedented structure and dynamics studies in biology and beyond. SLIM combines Zernike's phase contrast method by revealing the intrinsic contrast of transparent samples [1], with Gabor's holography [26] by rendering *quantitative* phase maps across the sample.

Because of the extremely short coherence length of this illumination light, approximately 1.2 μm , SLIM provides speckle-free imaging with sub-nanometer *spatial* background noise. Further, the SLIM image is intrinsically registered with the other channels of the microscope, including fluorescence, which enables powerful multimodal investigations.

2. SLIM Setup

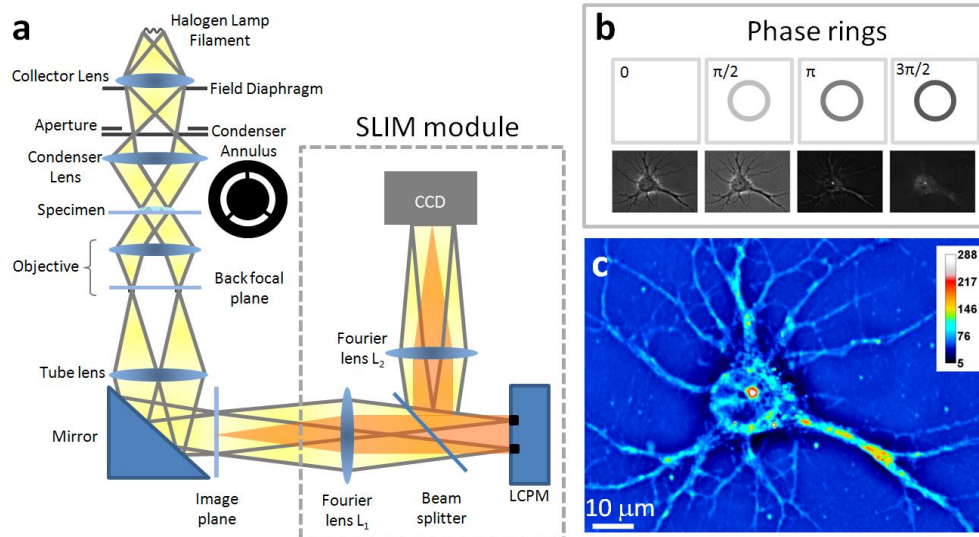


Fig. 1. SLIM principle. (a) Schematic setup for SLIM. The SLIM module is attached to a commercial phase contrast microscope (Axio Observer Z1, Zeiss, in this case). The lamp filament is projected onto the condenser annulus. The annulus is located at the focal plane of the condenser, which collimates the light towards the sample. For conventional phase contrast microscopy, the phase objective contains a phase ring, which delays the unscattered light by a quarter wavelength and also attenuates it by a factor of 5. The image is delivered via the tube lens to the image plane, where the SLIM module processes it further. The Fourier lens L_1 relays the back focal plane of the objective onto the surface of the liquid crystal phase modulator (LCPM, Boulder Nonlinear). By displaying different masks on the LCPM, the phase delay between the scattered and unscattered components is modulated accurately. Fourier lens L_2 reconstructs the final image at the CCD plane, which is conjugated with the image plane. (b) The phase rings and their corresponding images recorded by the CCD. (c) SLIM quantitative phase image of a hippocampal neuron.

A schematic of the instrument setup is depicted in Fig. 1a. SLIM was developed by producing additional spatial modulation to the image field outputted by a commercial phase contrast microscope. Specifically, in addition to the $\pi/2$ shift introduced in phase contrast between the scattered and unscattered light from the sample [1], we generated further phase shifts, by increments of $\pi/2$, and recorded additional images for each phase map. Thus, the objective exit pupil, containing the phase shifting ring, is imaged via lens L_1 onto the surface of a reflective liquid crystal phase modulator (LCPM, Boulder Nonlinear). The active pattern on the LCPM is calculated to precisely match the size and position of the phase ring image, such that additional phase delay can be precisely controlled between the scattered and unscattered components of the image field. In this setup, 4 images corresponding to each phase shift are recorded (Fig. 1b), to produce a *quantitative phase image* that is uniquely determined (see LCPM calibration Section below). Figure 1c depicts the quantitative phase image associated with a cultured hippocampal neuron, which is proportional to

$$\phi(x, y) = \frac{2\pi}{\lambda} \int_0^{h(x,y)} [n(x, y, z) - n_0] dz. \quad (1)$$

In Eq. (1), $n-n_0$ is the local refractive index contrast between the cell and the surrounding culture medium, h the local thickness of the cell, and λ the central wavelength of the illumination light. SLIM provides the local phase shift ϕ with great accuracy, which in turn allows for detecting local changes in thickness h at a scale much smaller than the wavelength of light. The typical irradiance at the sample plane is $\sim 1 \text{ nW}/\mu\text{m}^2$. The exposure time was 10–50 ms, for all the images presented in the manuscript. This level of exposure is 6–7 orders of magnitude below that of typical confocal microscopy [27], which allows for noninvasive live-cell imaging over extended periods of time (many hours or days).

3. Liquid crystal phase modulation

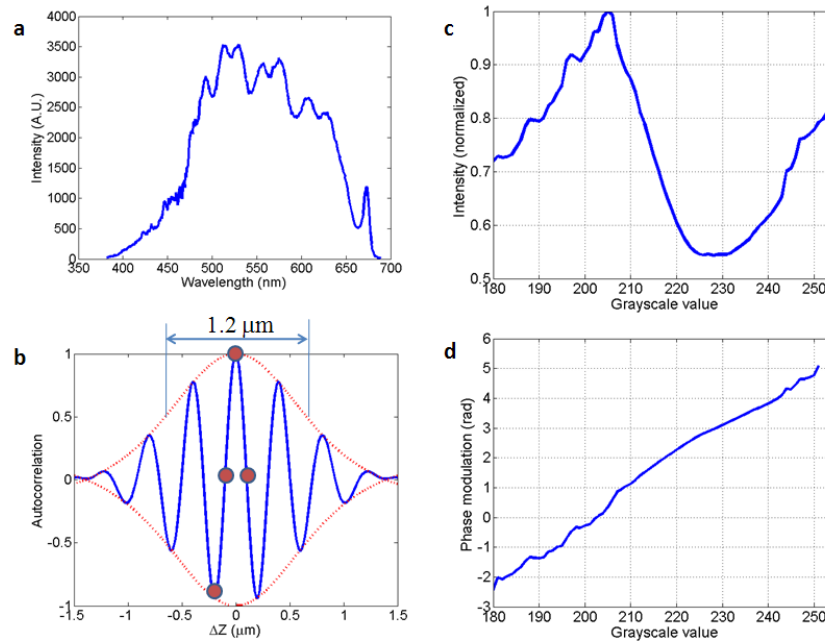


Fig. 2. (a) Spectrum of the white light emitted by the halogen lamp. The center wavelength is 552.3 nm. (b) The autocorrelation function (blue solid line) and its envelope (red dotted line). The 4 circles indicate the phase shifts produced by LCPM. The refractive index of the medium is 1.33. (c). Intensity modulation obtained by displaying different grayscale values on the LCPM. (d) Phase vs. gray scale calibration curve obtained by Hilbert transform of the signal in (c).

Using a spectrometer (USB 2000, Ocean Optics, USA), we measured the optical spectrum of the illuminating white light at the CCD plane. This spectrum is shown in Fig. 2a. From these data, we retrieved the temporal autocorrelation function of the light via a Fourier transform (Fig. 2b). The spectrum provided by the spectrometer is sampled in wavelength. In order to obtain the spectrum vs. frequency, which then can be Fourier transformed, we performed resampling of the data. In a medium of refractive index $n = 1.33$ (i.e. water), the coherence length defined at full width half maximum is $l_c^{FWHM} = 1.2 \mu\text{m}$. This coherence length is at least an order of magnitude shorter than that of other light sources such as broadband lasers, light emitting diodes and superluminescent diodes. However, within this coherence length there are still several full cycle modulations. Thus, the envelop varies slowly over one period near the central peak, which enables the application of the phase shifting procedure described below.

The LCPM (XY Phase Series Model P512 –635, Boulder Nonlinear Systems, Inc, USA) was calibrated to decide the relationship between pixel grey values fed via a VGA signal to the liquid crystal array and the final phase delay introduced to the unscattered field. The LCPM was placed between two polarizers and its intensity transmission was recorded as

follows. We first changed the polarizer and analyzer by 45° so that SLIM will work in “amplitude modulation” mode. Then we scanned through the grayscale value from 128 to 255 (i.e. 8 bits). The modulation from pixel value 0 to 127 and from 128 to 255 is symmetric. Thus we only need to scan half of the pixel values. The intensity transmitted through the LCPM vs. the grey value is shown in Fig. 2c. From the amplitude response of the modulator we obtained its phase response via a Hilbert transform, as shown in Fig. 2d.

For spatial coherent imaging system, after passing the specimen, a portion of the light remains unscattered and forms a uniform background of the image; the other portion is scattered and contains the fine structure information of the specimen. If we denote the unscattered light as U_0 and the scattered light field as $U_1(x, y)$, the intensity at CCD is

$$I(x, y; \varphi) = |U_0|^2 + |U_1(x, y)|^2 + 2|U_0||U_1(x, y)|\cos[\Delta\phi(x, y) + \varphi], \quad (2)$$

where $\Delta\phi(x, y)$ is the phase difference between U_0 and $U_1(x, y)$, and φ is the additional phase modulation introduced by LCPM, as shown in Fig. 2. Note that for $\varphi = \pi/2$, traditional phase contrast is obtained.

The quantity of interest $\Delta\phi(x, y)$ is retrieved as

$$\Delta\phi(x, y) = \tan^{-1} \left[\frac{I(x, y; -\pi/2) - I(x, y; \pi/2)}{I(x, y; 0) - I(x, y; \pi)} \right]. \quad (3)$$

If we define $\beta(x, y) = |U_1(x, y)|/|U_0|$, then the phase associated with the image field $E(x, y)$ can be determined [11,28]:

$$\phi(x, y) = \tan^{-1} \left[\frac{\beta(x, y) \sin(\Delta\phi(x, y))}{1 + \beta(x, y) \cos(\Delta\phi(x, y))} \right]. \quad (4)$$

Note that ϕ defines the phase delay associated with the autocorrelation function depicted in Fig. 2b.

4. Nanoscale topography with SLIM

In order to assess the spatial accuracy of SLIM, we imaged an amorphous carbon film deposited on glass and compared the topography measurements against atomic force microscopy (AFM). The topography measurements by SLIM and AFM, respectively, are summarized in Fig. 3a and 3b. The two types of measurement agree within a fraction of a nanometer. Note that both SLIM and AFM are characterized by much smaller errors than suggested by the widths of the histogram modes, as these widths also reflect irregularities in the surface topography due to the fabrication process itself. Of course, AFM is not limited by diffraction in the transverse direction. Unlike AFM, SLIM is non-contact, parallel, and faster by more than 3 orders of magnitude. Thus, SLIM can optically measure an area of $75 \times 100 \mu\text{m}^2$ in 0.5 s compared to a $10 \times 10 \mu\text{m}^2$ field of view measured by AFM in 21 minutes.

As further comparison, we evaluated background images (*i.e.*, no sample) from SLIM and diffraction phase microscopy (DPM) [9], an established laser-based technique that was interfaced with the same microscope (Fig. 3d and 3e). Due to the lack of speckle effects granted by its broad spectral illumination, SLIM’s spatial uniformity and accuracy for structural measurements is substantially better than DPM’s. To quantify the spatio-temporal phase sensitivity, we imaged the SLIM background repeatedly to obtain a 256-frame stack. Figure 3f shows the spatial and temporal histograms associated with the optical path-length shifts across a $10 \times 10 \mu\text{m}^2$ field of view and over the entire stack, respectively. These noise levels, 0.3 nm and 0.03 nm, represent the limit in optical path-length sensitivity across the image and between frames, respectively. The diminished effects of speckles allowed quantitative phase imaging to reveal single atomic layers of carbon, for the first time [29].

Several error sources can potentially be diminished further: residual mechanical vibrations in the system that are not “common path”, minute fluctuations in the intensity and spectrum of the thermal light source, digitization noise from the CCD camera (12 bit in our case), and the stability (repeatability) of the liquid crystal modulator (8 bit).

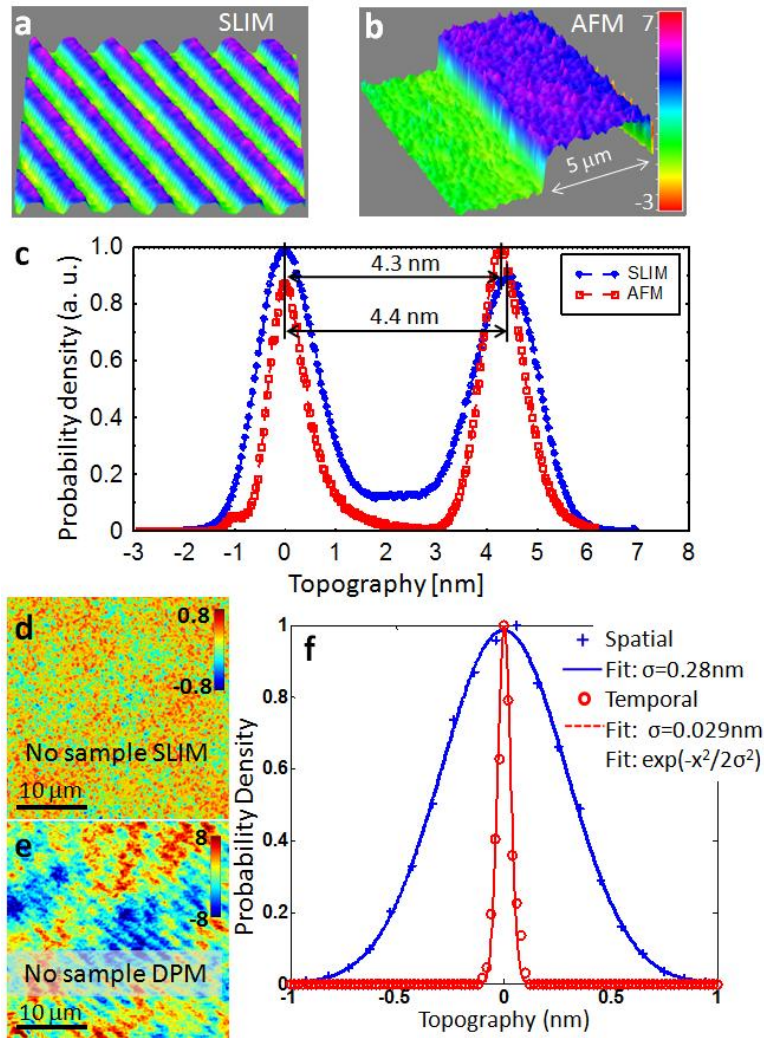


Fig. 3. Comparison between SLIM and AFM. (a) SLIM image of an amorphous carbon film. (b) AFM image of the same sample, with the colorbar indicating thickness in nm. (c) Topographical histogram for AFM and SLIM, as indicated. (d) Topography noise in SLIM; color bar in nanometers. (e) Topography noise associated with diffraction phase microscopy, a laser-based technique; color bar in nanometers. (f) Optical path-length noise level measured spatially and temporally, as explained in text. The solid lines indicate Gaussian fits, with the standard deviations as indicated.

The LCPM maximum refresh rate is 60 Hz, in principle allowing for 15 SLIM images per second but throughout the manuscript we report imaging at 2.6 frames/ s, as our camera has a maximum acquisition rate of 11 frames/s at full resolution. Acquisition speed could be increased to video rate by employing a faster phase modulator and camera.

5. Multimodal SLIM-fluorescence imaging

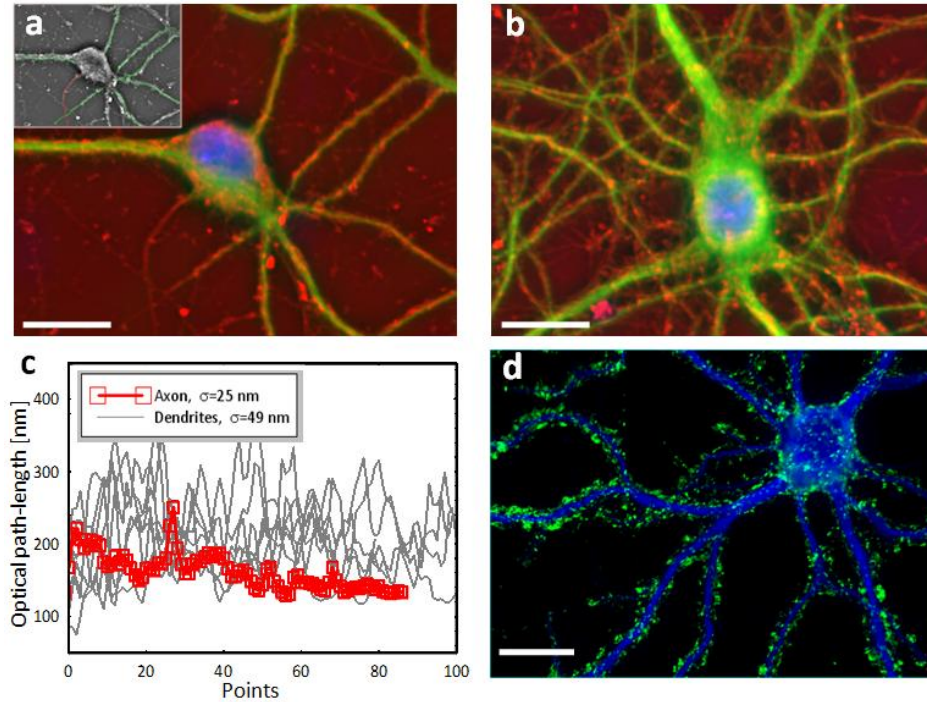


Fig. 4. SLIM-fluorescence multimodal imaging. (a)-(b) Combined multimodal images of cultured neurons (19 DIV) acquired through SLIM (red) and fluorescence microscopy of anti-MAP2 stained soma and dendrites (green) and DAPI-stained nuclei (blue). (c) Optical path-length fluctuations along the dendrites (green) and axon (red) retrieved from the inset of (a). (d) Synaptic boutons of a mature hippocampal neuron (33 DIV) immunochemically labeled for synapsin (green) and MAP2 (blue). Scale bars: 20 μm .

A distinct feature of SLIM is that the quantitative phase image is overlaid with the other imaging channels of the microscope, such as epi-fluorescence, differential interference contrast, and phase contrast. Simultaneous fluorescence imaging complements SLIM's structural information with the ability to study cellular constituents with molecular specificity. In Fig. 4a and 4b, we show multimodal SLIM-fluorescence imaging of primary hippocampal neurons cultured for 19 days *in vitro* (DIV). Nucleus (blue) and dendrites (green) are stained by 4',6-diamidino-2-phenylindole (DAPI) and the somatodendritic marker microtubule-associated protein 2 (MAP2), respectively. The red line in the inset of Fig. 4a indicates the axon, as evidenced by the absence of MAP2 staining.

In order to quantify the structures observed by SLIM, we traced individual neurites using NeuronJ (Fig. 4c). Each trace shows the optical path-length fluctuations along each different neurite. The standard deviation (σ) of the path-length fluctuation is, on average, twice as large for dendrites as it is for the axon, *i.e.*, 49 nm vs. 25 nm. This result suggests that subtle inhomogeneities are associated with the synaptic structures and these inhomogeneities can be revealed by SLIM as path-length changes. By 3 weeks in dispersed culture, the majority of dendritic spines generally mature to form presynaptic boutons on the dendritic shafts. After 33 DIV, we observe synapsin and MAP2 labeling of putative synaptic elaborations on a mature hippocampal neuron (Fig. 4d).

From the quantitative phase measured, other representations of the information can be obtained numerically. Thus, the spatial gradient of the SLIM image simulates DIC microscopy in Fig. 5c (Media 1). Further, we show that the Laplacian of the image, a second

order derivative operation, is even more powerful than DIC in revealing fine structures within the cell, as it does not contain significant shadow artifacts in Fig. 5d (Media 1).

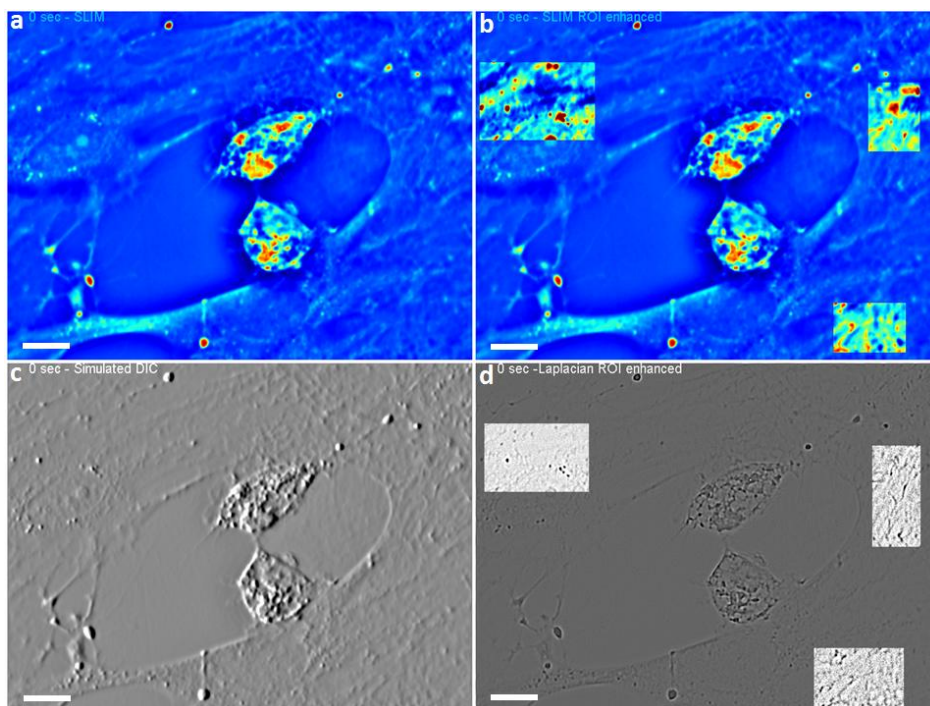


Fig. 5. (Media 1) SLIM simulated DIC and Laplacian. Since the quantitative phase information is obtained, all other microscopy such as DIC, phase contrast and dark field can be numerically simulated through SLIM imaging. Objective: Zeiss EC Plan-Neofluar $40\times/0.75$. (a) SLIM imaging of glial-microglia cell culture. (b) SLIM imaging with ROI (region of interest) enhancement. (c) Simulated DIC-based on the phase measurement of SLIM. (d) Laplacian of SLIM image with ROI enhancement. Scale bars: 10 μm .

6. Cell dynamics measurements

Due to the extremely low level of spatial noise (0.3 nm) and temporal stability (0.03 nm), SLIM is able to image sub-nanometer dynamics in live cells for periods ranging from seconds to days. For example, we obtained 397 two-dimensional SLIM images of a mixed glial-microglial cell culture over 13 minutes (Fig. 6). When we compare live-cell measurements made by phase contrast vs. SLIM imaging, significant differences are apparent. The cell size is clearly overestimated by phase contrast due to the well known halo artifact which makes the borders of the cell appear bright (Fig. 6b). Also, the conventional phase contrast images extracted from these data are unable to provide quantitative information about dynamic changes in optical path-length (Fig. 6b and 6c). Importantly, due to the contrast change of the halo with the phase shift (Fig. 1b), SLIM is able to minimize this effect when combining the four phase ring frames (Fig. 6d).

Path-length changes due to both membrane displacements and local refractive index changes caused by cytoskeleton dynamics and particle transport at two arbitrary points on the cell reveal an interesting, periodic behaviour (Fig. 6d, 6f). At different sites on the cell, the rhythmic motions have different periods, which may indicate different rates of metabolic or phagocytic activity. This periodicity can be observed in coordinated cell behaviour as the cell extends broad, dynamic filopodial ruffles under, and above, the neighbouring glial cells in Fig. 6 (Media 2).

Because of the extremely low noise level of SLIM, the probability distribution of path-length displacements between two successive frames was retrieved with a dynamic range of

over 5 orders of magnitude (Fig. 6g). This distribution can be fitted very well with a Gaussian function up to path-length displacements $\Delta s = 10$ nm, at which point the curve crosses over to an exponential decay. The normal distribution suggests that these fluctuations are the result of numerous uncorrelated processes governed by equilibrium. On the other hand, exponential distributions are indicative of deterministic motions, mediated by metabolic activity.

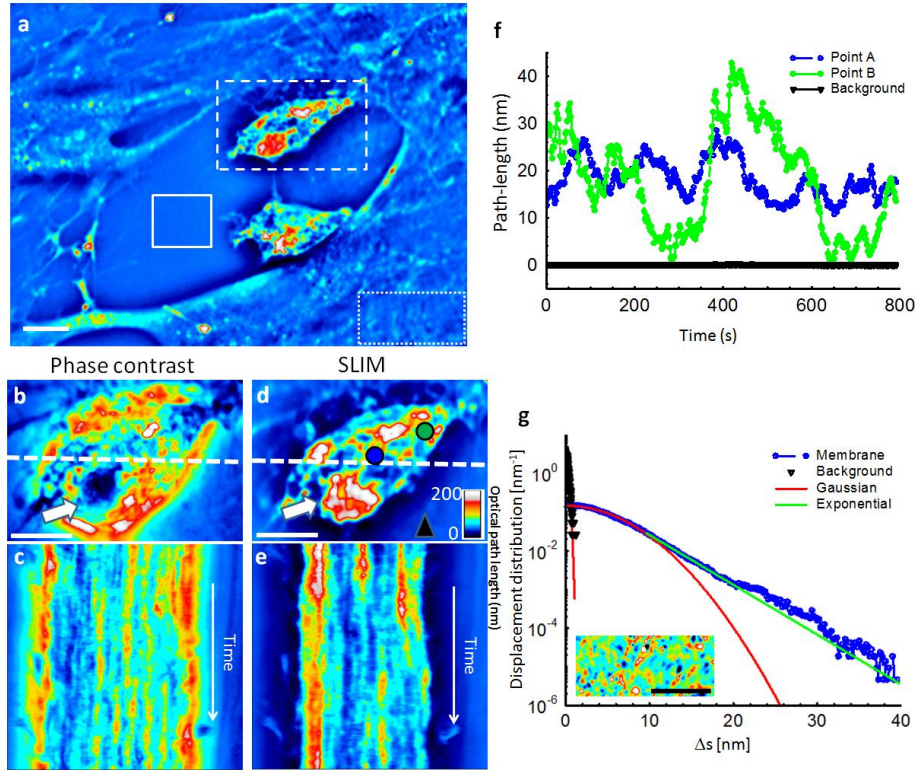


Fig. 6. (Media 2) SLIM dynamic imaging of mixed glial-microglial cell culture. Two reactive microglia probe neighboring cellular environments with highly dynamic lamellipodia and begin engulfing matter through long, thin projections in serum-starved primary mixed glial cultures. Actin polymerization and depolymerization are evident in the membrane area. SLIM reveals changes in optical path length of these dynamic cellular behaviors. Objective: Zeiss EC Plan-Neofluar $40 \times /0.75$. (a) Phase map of two microglia cells active in a primary glial cell culture. Solid line box indicates the background used in (g), dashed line box delineates a reactive microglial cell used in (b)-(e) and dotted line box indicates the glial cell membrane used in (g). (b) Phase contrast image of the cell shown in (a). pseudocoloration is for light intensity signal and has no quantitative meaning for phase contrast. (c) Registered time-lapse projection of the corresponding cross-section through the cell as indicated by the dash line in (b). (d) SLIM image of the cell in (b); the fields of view are the same. The arrows in (b) and (d) point to the nucleus which is incorrectly displayed by phase contrast as a region of low signal. (e) Registered time-lapse projection of the corresponding cross-section through the cell, as indicated by the dash line in (d). (f) Path-length fluctuations of the points on the cell (indicated in d) showing intracellular motions (blue- and green-filled circles). Background fluctuations (black) are negligible compared to the active signals of the microglia. (g) Semi-logarithmic plot of the optical path-length displacement distribution associated with the glial cell membrane indicated by the dotted box in (a). The solid lines show fits with a Gaussian and exponential decay, as indicated in the legend. The distribution crosses over from a Gaussian to an exponential behavior at approximately 10 nm. The background path-length distribution, measured from the solid line box, has a negligible effect on the signals from cells and is fitted very well by a Gaussian function. The inset shows an instantaneous path-length displacement map associated with the membrane. Scale bars, 10 μm (a), (b), (d) and (g).

SLIM studies of cell dynamics should reveal previously unknown information regarding membrane motions, cytoskeleton mechanics, and particle transport within the cell. Figure 7

(Media 3) shows SLIM imaging of neuron processes, which suggests that SLIM may offer a window into studying the dynamic processes associated with the formation and transition of collateral filopodia into spines, and the dynamics of plasticity-related changes in spine structure [30]. Note that SLIM can be used to image cellular dynamics, including bidirectional neurite transport and actin dynamics over extended periods of time without loss in performance.

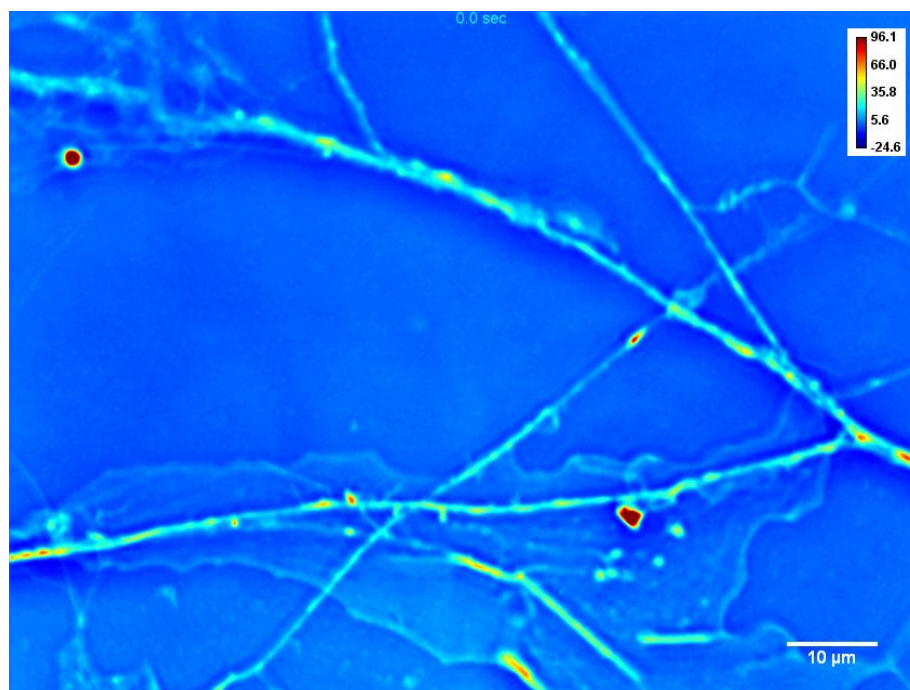


Fig. 7. (Media 3) SLIM imaging of live hippocampal neuron. in primary cell culture. Through SLIM bidirectional microtubule-mediated transport is prominently evident in neurites, individually or in neurite bundles. Slower dynamic leading edges of advancing glial membranes expand short distances across the coverslip. Actin polymerization and depolymerization are evident in the membrane area. SLIM reveals changes in optical path length of these dynamic cellular behaviors. Colorbar indicates path-length in nm. Objective: Zeiss Plan-Apochromat 63 × /1.4 Oil.

7. Summary and outlook

In sum, our results demonstrate that rich and quantitative information can be captured from biological structures using SLIM without physical contact or staining. The main features associated with SLIM are as follows. SLIM provides speckle-free images, which allows for *spatially* sensitive optical path-length measurement (0.3 nm). It uses common path interferometry, which enables *temporally* sensitive optical path-length measurement (0.03nm). Our initial results demonstrate that rich, previously unobservable information can be captured in the spatially-resolved cell phase shift map as demonstrated by neuron imaging. The co-registration with the fluorescence channels of the microscope represents a significant feature, which enables in-depth biological studies. Finally, the broadband illumination field offers opportunities for spectroscopy, as recently demonstrated in a different configuration [31]. The authors are optimistic about SLIM having a major impact in the field of light microscopy, as existing phase contrast microscopes can be converted easily (via an add-on module) to provide quantitative and nanoscale information.

Acknowledgments

This study was supported by the National Science Foundation (CAREER 08-46660 to GP), the Grainger Foundation (to GP), and the National Institute of Mental Health (R21 MH085220 to MUG). LM was supported by the National Institute of Child Health and Human Development Developmental Psychobiology and Neurobiology Training Grant (HD007333). ZW and GP acknowledge visualization tools by Ethan Berl and stimulating discussions with Dan Marks and Scott Carney. Related information can be found at <http://light.ece.uiuc.edu/>.